

See discussions, stats, and author profiles for this publication at: <https://www.researchgate.net/publication/272513749>

# Graphene Aerogel/Epoxy Composites with Exceptional Anisotropic Structure and Properties

ARTICLE in ACS APPLIED MATERIALS & INTERFACES · FEBRUARY 2015

Impact Factor: 6.72 · DOI: 10.1021/acsami.5b00146 · Source: PubMed

CITATIONS

9

READS

89

8 AUTHORS, INCLUDING:



Xi Shen

The Hong Kong University of Science and Tec...

17 PUBLICATIONS 336 CITATIONS

SEE PROFILE



Xiuyi Lin

The Hong Kong University of Science and Tec...

15 PUBLICATIONS 468 CITATIONS

SEE PROFILE



Jang Kyo Kim

The Hong Kong University of Science and Tec...

315 PUBLICATIONS 8,197 CITATIONS

SEE PROFILE

# Graphene Aerogel/Epoxy Composites with Exceptional Anisotropic Structure and Properties

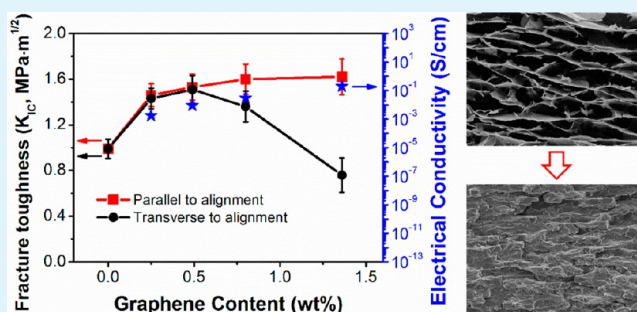
Zhenyu Wang, Xi Shen, Mohammad Akbari Garakani, Xiuyi Lin, Ying Wu, Xu Liu, Xinying Sun, and Jang-Kyo Kim\*

Department of Mechanical and Aerospace Engineering, The Hong Kong University of Science and Technology, Clear Water Bay, Kowloon, Hong Kong

## S Supporting Information

**ABSTRACT:** 3D interconnected graphene aerogels (GAs) are prepared through one-step chemical reduction and rational assembly of graphene oxide (GO) sheets, so that the difficulties to uniformly disperse the individual graphene sheets in the polymer matrixes are avoided. Apart from ultralow density, high porosity, high electrical conductivity, and excellent compressibility, the resulting GAs possess a cellular architecture with a high degree of alignment when the graphene content is above a threshold,  $\sim 0.5$  wt %. The composites prepared by infiltrating GA with epoxy resin present excellent electrical conductivities, together with high mechanical properties and fracture toughness. The unusual anisotropic structure gives rise to  $\sim 67\%$  and  $\sim 113\%$  higher electrical conductivity and fracture toughness of the composites, respectively, in the alignment direction than that transverse to it.

**KEYWORDS:** graphene aerogel, reduced graphene oxide, nanocomposite, anisotropic properties



## 1. INTRODUCTION

Graphene, a two-dimensional, one-atomic thick carbon material, has played a central role in the coming era of nanotechnology due to its exceptional physical, chemical, and mechanical properties.<sup>1,2</sup> To harness the excellent nanoscale properties for macroscopic applications, one of the most efficient ways is to incorporate graphene into polymers to make composites.<sup>3</sup> Graphene oxide (GO), as a derivative of graphene, has excellent solubility in aqueous media due to the oxygenated functional groups on its surface, making it an ideal nanofiller to prepare composites. GO and reduced GO (rGO) have been incorporated into a wide range of polymer matrixes using several methods, like solvent mixing, *in situ* polymerization, and melt processing, for various functional and structural applications.<sup>4–7</sup> To fully utilize the potentials of graphene as a superior functional filler, many efforts have been made to resolve several key issues, such as alignment of graphene in polymer,<sup>7,8</sup> uniform dispersion,<sup>9,10</sup> and surface modifications.<sup>11,12</sup> Although many improvements have been achieved, the properties of the composites are still far from those anticipated from the inherent properties of graphene.

More recently, three-dimensional (3D) graphene materials in the form of graphene foam (GF), graphene hydrogel (GH), and graphene aerogel (GA) have emerged, offering totally new processing routes to fabricate composites with much enhanced properties.<sup>13,14</sup> Among them, GA, a porous 3D graphene material assembled by individual rGO sheets, has attracted tremendous attention for application in various areas, especially

as electrodes in electrochemical energy devices like rechargeable batteries, supercapacitors, and fuel cells.<sup>15,16</sup> GAs are normally prepared using a sol–gel process where 3D interconnected GH is formed via gelation of GO dispersion by adding cross-linkers, reducing agent, or treating at an elevated temperature and pressure using a hydrothermal method.<sup>17–20</sup> In addition, reducing agents, such as L-ascorbic acid and hydroiodic (HI) acid, are often added during or after the hydrothermal process to further improve the degree of reduction and thus the electrical conductivity of the final products.<sup>21,22</sup> The as-prepared GH is subsequently subjected to supercritical fluid drying or freeze-drying to replace the solvent with air to form GA with a highly porous structure. Apart from the intrinsic properties of 2D graphene sheets, GAs also possess useful attributes that other forms of 2D graphene structures lack, such as extremely large surface area, ultralow density, and excellent electrical and mechanical properties, making them an ideal filler for polymer composites.<sup>14,23,24</sup> In accordance with the end applications, different types of GA/polymer composites have been studied, namely porous and solid composites.<sup>25–30</sup> A typical method to prepare porous GA/polymer composites is to make GA/polymer hybrid aerogels by either direct freeze-drying of the GO/polymer precursor or coating polymers onto the walls of GAs. The resulting composites retain the porous

Received: January 6, 2015

Accepted: February 18, 2015

Published: February 18, 2015

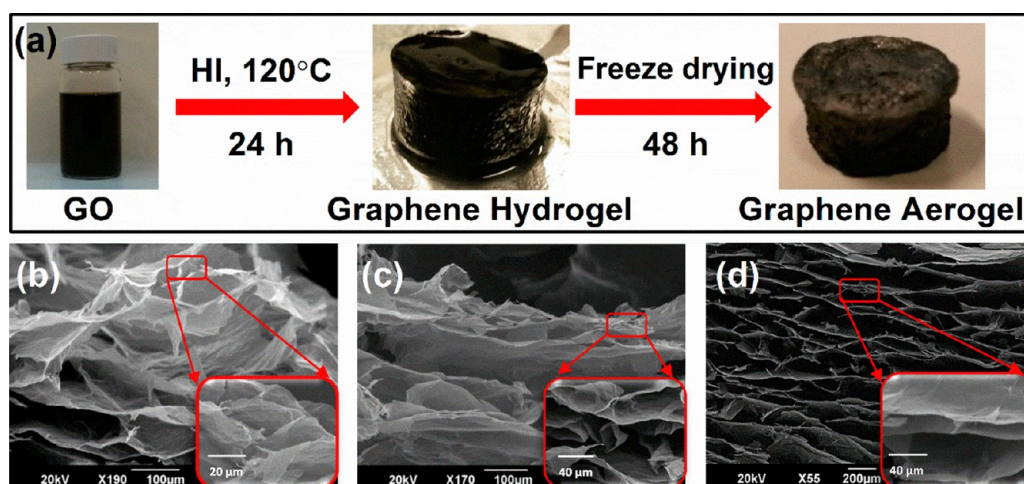


**Figure 1.** (a) Schematic illustration of the fabrication process of GA and SEM images of GAs prepared using GO dispersions at different concentrations of (b) 0.5, (c) 1.5, and (d) 2.0 mg/mL.

structure of GAs while they are significantly strengthened/stiffened due to the incorporation of polymer and possess multifunctional characteristics, such as superhydrophobicity and stimuli-responsiveness, depending on the type of polymers used.<sup>25–27</sup> Meanwhile, solid GA/polymer composites are prepared by infiltrating a liquid polymer into the porous network of GA, followed by curing or solidifying the polymer matrix. Using the 3D interconnected GA architecture, instead of individual GO sheets, as the reinforcement of composites means that the composite fabrication process does not require the complicated functionalization and dispersion of individual GO sheets before adding into the polymer matrix. Therefore, the solid composites reinforced with GAs exhibited superior mechanical properties, and electrical and thermal conductivities, as compared to those made from dispersed 2D graphene sheets.<sup>28–30</sup>

Herein, we report the synthesis of GAs through one-step chemical reduction and rational self-assembly of GO sheets using hydriodic (HI) acid, followed by freeze-drying. Apart from ultralow density, high porosity, high electrical conductivity, and excellent compressibility as in previous studies,<sup>17–22</sup> the GAs prepared in this work consist of a 3D interconnected rGO structure with significant alignment in one direction, giving rise to unique anisotropy between the properties measured in the orthogonal directions of GA as well as the corresponding GA/epoxy composites. To the authors' best knowledge, this work is the first of its kind to report anisotropic electrical, mechanical, and fracture properties of GA-based composites to such large extents, making them promising candidates for applications like anisotropic conductive adhesives and outer structures in multilayered biological systems.<sup>31,32</sup>

## 2. EXPERIMENTAL SECTION

**2.1. Synthesis of GAs and GA/Epoxy Composites.** GO dispersion was prepared on the basis of the modified Hummers method using natural graphite flakes (supplied by Asbury Graphite Mills) following our previous studies.<sup>33</sup> The resultant GO dispersion was diluted using deionized (DI) water and sonicated for 30 min in a bath sonicator. GHs were prepared by chemical reduction and self-assembly of GO sheets using hydriodic acid (HI, 57%, Acros) as the reducing agent. In a typical procedure, HI with a mass ratio of HI to GO = 3:1 was added into the GO dispersion at a concentration ranging from 0.3 to 2.0 mg/mL, which was mixed using a magnetic

stirrer for several minutes. It should be noted here that processing the GO dispersion with concentrations beyond 2.0 mg/mL was very difficult because of the drastically increased viscosity and thus serious agglomeration of the GO sheets in the final product. The mixture was then sealed in a Teflon-lined autoclave at 120 °C for 24 h, which was chosen as the optimized condition after extensive preliminary experiments to obtain GA with an acceptable degree of reduction. After being cooled to room temperature, the as-produced GH was washed using DI water for 24 h to fully remove the residual impurities. The GH was then stored at –30 °C for 12 h and freeze-dried at –80 °C for 48 h in a freeze drier (SuperModulyo, Thermo Fisher) to form GA. Digital images of GH and GA are shown in Figure 1a. The GA/epoxy composites were fabricated using a vacuum-assisted infiltration method, and the details can be found in the Supporting Information.

**2.2. Characterization and Mechanical Tests.** The morphology of GAs and fracture surface of GA/epoxy composites were examined on a scanning electron microscope (SEM, JEOL 6390F). Raman spectroscopy (Reinshaw MicroRaman/Photoluminescence System) was used to characterize the degree of reduction of GA, the GA/epoxy interfacial bonds, and the anisotropic nature of the composite. He–Ne laser with a wavelength of 632.8 nm was used in all experiments. X-ray photoelectron spectroscopy (XPS, Axis Ultra DLD) was used to study the elemental compositions of GO and GA. Fourier transform infrared spectroscopy (FTIR, Bio-Rad FTS 6000) was used to study the interfacial interactions of the composites in the near-infrared region (400–4000 cm<sup>–1</sup>), collecting attenuated total reflectance (ATR) spectra. Compression tests of GAs under cyclic loading were performed on a universal testing machine (Instron 5567) at a constant cross-head speed of 2.0 mm/min. The electrical conductivities of GAs and GA/epoxy composites were measured on the basis of the four-point probe method (Scientific Equipment & Services). To reduce the contact resistance between the probes and the sample surface, the contact points were coated with silver paste. The surface roughness,  $R_a$ , of the fracture surface of composites was determined using the optical surface profiler (Profilometer Tencor Alpha Step 200).

Flexural tests and fracture toughness tests were performed on a universal testing machine (MTS Alliance RT/5) at room temperature according to the specifications, ASTM D790 and ASTM D5045, respectively. In the flexural tests, 28 mm long × 3.0 mm wide × 1.6 mm thick specimens were loaded in three-point bending with a support span of 24 mm at a constant cross-head speed of 2.0 mm/min. In the fracture toughness tests, single edge notched bend (SENB) specimens of 28 mm long × 6 mm high × 3 mm thick were loaded in three-point bending at a span of 24 mm and a cross-head speed of 10.0 mm/min. The fracture specimens were precracked to a total crack length of 3 mm according to the previous studies.<sup>34,35</sup> The fracture toughness,  $K_{IC}$ , under the plane strain condition was calculated using the following equations:<sup>35</sup>



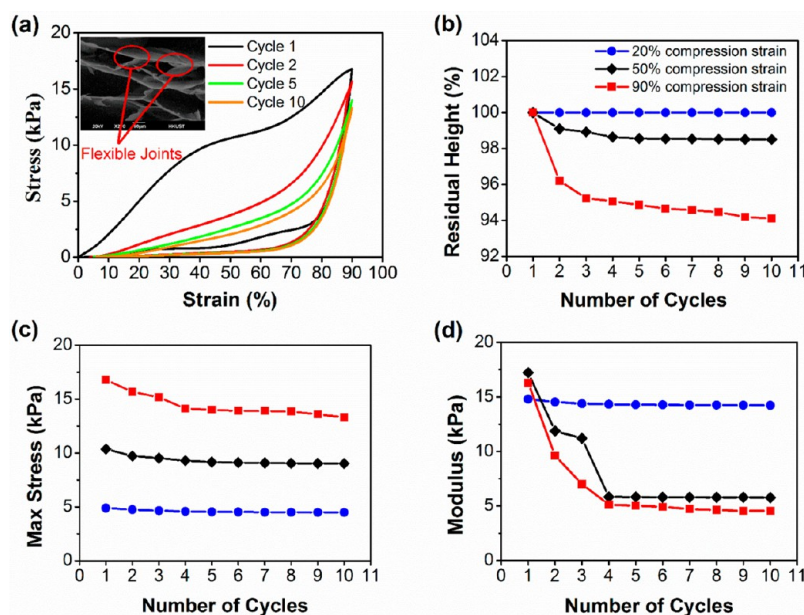


**Figure 2.** Compression properties of GAs prepared using a GO dispersion of concentration 2.0 mg/mL: (a) stress–strain curves of GAs to a maximum strain of 90% for 10 cycles; (b) residual height; (c) maximum stress; and (d) compressive modulus measured at different maximum strains of 20%, 50%, and 90% as a function of number of cycles.

$$K_{IC} = \frac{P_{max}f(x)}{BW^{1/2}}, \quad x = a/W \quad (1)$$

$$f(x) = 6x^{1/2} \frac{[1.99 - x(1-x)(2.15 - 3.93x + 2.7x^2)]}{(1+2x)(1-x)^{3/2}} \quad (2)$$

where  $P_{max}$  is the maximum load,  $B$  and  $W$  are the width and height of the specimen, and  $a$  is the initial crack length. Note that in all samples, the term  $a/W$  was equal to  $\sim 0.5$ , and the above specimen dimensions satisfied the requirement for plane strain conditions. At least five samples were tested in both the flexural and the fracture tests.

### 3. RESULTS AND DISCUSSION

**3.1. 3D Interconnected Layered Structure of GA.** In a typical synthesis process of GA, the GO and HI acid mixture was hydrothermally treated at 120 °C to transform to hydrogel, which was then freeze-dried to form GA as illustrated in Figure 1a. The GO sheets used here to prepare GAs had areas ranging from a few to a few hundred square micrometers with a mean area of 202  $\mu\text{m}^2$ , as shown in Supporting Information Figure S2.<sup>33,36</sup> The GO sheets were well dispersed in water to form a stable dark brown colloidal dispersion (Figure 1a), thanks to the electrostatic repulsion between them resulting from the ionized carboxyl groups. GO sheets were then reduced by HI acid, leading to strong  $\pi$ – $\pi$  interactions between the rGO layers, which facilitated self-assembly into the black GH monolith. The freeze-dried GA possessed a 3D porous network with interconnected pores ranging from tens to over a hundred of micrometers, as shown in SEM images (Figure 1b–d). Interestingly, GAs made from low concentration graphene exhibited well exfoliated and randomly distributed rGO sheets (Figure 1b), whereas with an increase in GO concentration, the rGO sheets tended to align to form a layered structure. The aligned structure obtained at high GO concentrations consisted of long horizontal layers with bundles of rGO sheets loosely assembled together, which were vertically connected by shorter bridging sheets (see insets of Figure 1c,d). Several mechanisms were proposed previously to explain the alignment of well-

dispersed individual rGO sheets in a polymer matrix or solvent. They include ultralarge size GO sheets, low viscosity aqueous system, steric hindrance between the rGO sheets, and the excluded volume principle.<sup>7,37,38</sup> At a low concentration, rGO sheets tended to form a uniform-size porous structure to increase the entropy of the system while minimizing the free energy. In contrast, at a high concentration where the steric hindrance and  $\pi$ – $\pi$  interactions between the rGO sheets as well as the excluded volume concept prevail, the large size rGO sheets tended to self-align, whereas the smaller ones assembled in a random direction. In addition, the ice crystals grew preferentially along the horizontal direction during the freeze-drying process, which may also be partly responsible for the formation of the anisotropic morphology. On the basis of a previous study,<sup>39</sup> for the system containing different sizes of rGO sheets, the horizontally aligned larger sheets may significantly lower the ice front velocity, resulting in an anisotropic growth of ice crystals in the perpendicular directions. Therefore, the pores were much longer in the horizontal direction than in the transverse direction (Figure 1d).

The results obtained from the cyclic compression tests of GAs prepared from GO dispersions of 2.0 mg/mL in concentration are shown in Figure 2. The stress–strain curves (Figure 2a) present an approximately linear stress–strain response until the strain reached about 35%, which was followed by a relatively plateau region resulting from yielding of the vertically interconnected graphene sheets. The stress increased rapidly afterward, a reflection of diminishing pore volume. After the first cycle, the stress–strain curves changed drastically, showing much lower stress levels in the loading curves with gradually larger elastic region for up to 60–70% of strains, indicating initial permanent deformation of the structure in the first few cycles. However, the stress–strain curves were maintained steady thereafter, a reflection of the excellent compressibility benefited from the flexible joints in the structure (see inset of Figure 2a). It has been reported that the

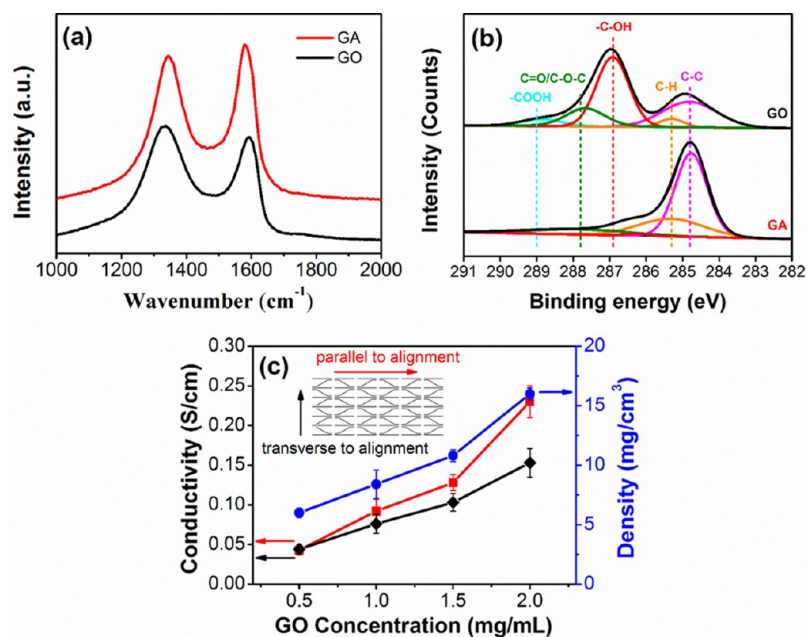


**Figure 3.** (a) Raman spectra D- and G-band peaks of GO and GA, (b) XPS C 1s deconvoluted spectra of GO and GA, and (c) electrical conductivities and density of GA in the direction parallel to the alignment and transverse to it as a function of GO concentration.

rGO films reduced by HI acid showed much better strength and flexibility than those reduced by other reducing agents, such as hydrazine and sodium borohydride ( $\text{NaBH}_4$ ).<sup>40</sup> The flexible joints consisted of short vertical sheets overlapped with the long horizontal layers of flexible rGO, capable of sustaining repeated cyclic deformation by bending under compression.

The corresponding responses of GAs to compression in terms of residual height, maximum stress, and compressive modulus are shown in Figure 2b–d. The residual height for each cycle was measured according to the height of initial loading location recorded by the universal testing machine. All of these properties remained largely unchanged regardless of cycles when only a 20% strain was applied. When the maximum strain was increased to 50% and 90%, however, there were large reductions in modulus for up to four cycles, followed by almost saturated moduli with further cyclic loading. The consistently reduced loading capacity for samples loaded at high strains was in connection with the yielding at strains typically around 35% as discussed above. According to previous studies, the yielding of porous structure was strongly associated with the progressive collapse of the pore cells by plastic deformation or brittle crushing.<sup>41</sup> Therefore, at low compressive strains below ~35%, GA was able to maintain most of its loading capacity, corresponding to elastic cell edge bending or face stretching, whereas at high compressive strains (>35%), the first few cycles led to a plastic yielding and crushing of the pore walls and certain weakly bonded joints, giving rise to reductions in loading capacity. However, over 90% of the original height was recovered upon unloading after 10 cycles even at a 90% compressive strain, confirming that the GA had a stable framework.

### 3.2. Reduction of GO during GA Fabrication Process.

Gelation of GO dispersion occurs when the GO network in the solution is reinforced by enhanced bonding forces, such as  $\pi$ – $\pi$  interaction and hydrogen bonds, or weakened repulsion forces, like electrostatic repulsion.<sup>18</sup> In this study, gelation was achieved by gradually restoring the  $\pi$ – $\pi$  interaction among the rGO sheets during the treatment with HI at 120 °C for 24

h. The GA was subsequently assembled due to the formation of physical cross-links between the rGO sheets. To characterize the degree of reduction, the chemical attributes of GO and GA were analyzed by Raman and XPS spectroscopies, as shown in Figure 3a and b. The Raman G-band is active in  $\text{sp}^2$ -hybridized carbon-based materials, while the D-band is activated when the defects participate in the double resonance Raman scattering near the K point of the Brillouin zone. Thus, the D- to G-band peak intensity ratios,  $I_D/I_G$ , are often used to estimate the  $\text{sp}^2$  domain size of carbon.<sup>36</sup>  $I_D/I_G$  decreased from 2.75 to 1.44 after GO was assembled into GA, indicating the removal of oxygenated functional groups from the GO sheets and the recovery of the  $\text{sp}^2$  conjugated carbon structure. In addition, the G-band peak was down-shifted from 1593 to 1579, reflecting the recovery of the hexagonal network of carbon atoms. The XPS results (Figure 3b) confirmed the reduction of GO: the C/O ratio increased drastically from 2.2 for GO to 8.9 for the aerogel. The C 1s deconvoluted spectra of GO consisted of two main components arising from  $-\text{C}-\text{OH}$  (~286.9 eV) and  $\text{C}-\text{C}$  (~284.8 eV), and three minor components from  $\text{C}-\text{H}$  (~285.3 eV),  $\text{C}=\text{O}/\text{C}-\text{O}-\text{C}$  (~287.8 eV), and  $-\text{COOH}$  (~289.0 eV) groups. It is clearly seen that most  $-\text{C}-\text{OH}$  and  $\text{C}=\text{O}/\text{C}-\text{O}-\text{C}$  functional groups on the GO basal plane and edges were eliminated by the GA fabrication process. In view of the above observations, it is clear that GO was partially reduced to rGO in GA. However, the remaining small amount of functional groups on rGO may contribute to enhancing the rGO–epoxy interfacial bonds and thus the mechanical properties of the composites; see section 3.4. It is worth noting that the C/O atomic ratio of GAs obtained in this work was generally higher than those of the GAs made by others using similar low-temperature processes, that is, C/O ratio = 8.9 (in this study) versus 5.3<sup>20</sup> or 8.69.<sup>42</sup> It should also be noted that GAs can be further reduced to enhance the C/O ratio by additional high temperature treatments.<sup>43</sup>

Hydrohalic acids, including HI, HBr, and HCl, are widely utilized in synthetic chemistry for the electrophilic addition and nucleophilic substitution reactions. The halides are nucleophilic



in nature, with increasing nucleophilicity in the order of  $\text{Cl}^- < \text{Br}^- < \text{I}^-$ , which makes HI an excellent candidate for removing the oxygenated functional groups abundant on the GO sheets.<sup>44</sup> The reduction mechanisms were studied by evaluating the chemical states of the residual iodine present on GA. After the GA fabrication, the I/C atomic ratio was only  $\sim 6.16 \times 10^{-3}$  (see Supporting Information Table S1), indicating that the iodine participating in the reduction reaction was removed from GA, instead of accumulating within GA. According to the XPS I 3d<sub>5/2</sub> peak (Supporting Information Figure S3b), the residual iodine is present mainly in two states: neutral iodine ( $\text{I}_2$  at  $\sim 620$  eV with  $\sim 68.4\%$ ) and the iodine anion ( $\text{I}^-$  at 619 eV with  $\sim 31.6\%$ ). In view of the ratio of  $\text{I}_2$  to  $\text{I}^-$  being approximately 2, it can be seen that  $\text{I}_2$  are assembled to form  $\text{I}_5^-$  after the iodine anions are oxidized to neutral iodine atoms by the oxygenated functional groups on GO sheets. Along with  $\text{I}_3^-$ ,  $\text{I}_5^-$  is known to be the stable state of iodine atoms in solution.<sup>40</sup> Therefore, according to the above discussion, possible reduction mechanisms are illustrated in Figure 4.

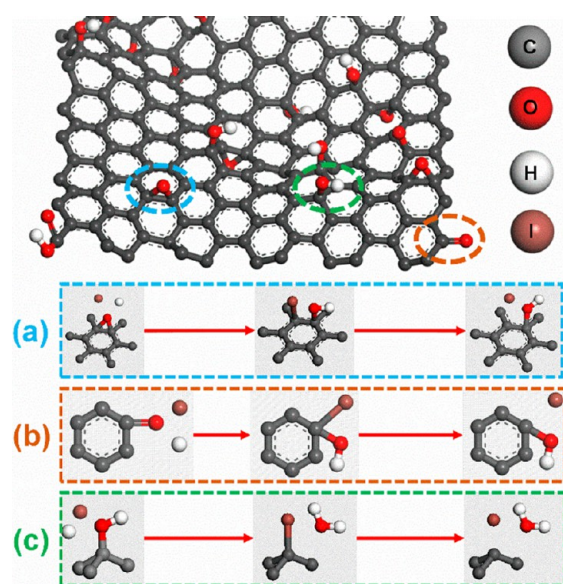


**Figure 4.** Schematic illustration of the elimination of oxygenated functional groups on GO by HI during the GA fabrication process: (a) epoxy, (b) carbonyl, and (c) hydroxyl functional groups.

Epoxy groups on the basal plane and carbonyl groups on the edge of GO sheets were reduced through the ring-opening reactions and addition reactions, which were then converted to hydroxyl groups (Figure 4a and b, respectively). The hydroxyl groups were further reduced by halogenation substitution reactions and transformed into carbon–iodine (C–I) groups (Figure 4c). The C–I bonds, as the intermediates in the reduction reactions, have the lowest binding energy among the carbon–halogen bonds, even lower than that of the C–H bonds, so that they can be easily removed from the basal plane in the form of iodine atoms.<sup>40,45,46</sup> The iodine atoms were further assembled with the iodine anions to form polyiodides,  $\text{I}_5^-$ , which were stably dissolved in the solution. The elimination of iodine was confirmed by the sharp decrease in I 3d peak after washing with water as highlighted in Supporting Information Figure S3a.

The resulting GAs delivered excellent electrical conductivities as high as 0.25 S/cm versus  $(5\text{--}16) \times 10^{-5}$  S/cm for the GO sheets,<sup>36</sup> proving almost full recovery of the conductivity after

reduction (Figure 3c). The electrical conductivities in both directions significantly increased with rising GO concentration, resulting from the formation of progressively denser conductive networks as evidenced by the functionally similar rising trend of the density of GAs. The anisotropic structure of GA is clearly manifested by the gradually larger disparity in conductivity between the directions of alignment and transverse to it.

### 3.3. Electrical Properties of GA/Epoxy Composites.

With high aspect ratios and exceptional electron mobility, graphene has been extensively explored to make high-performance conductive polymer composites. However, the electrical conductivities of graphene/polymer nanocomposites prepared by direct dispersion of few-layer graphene nanoplatelets (GNPs) or rGO sheets into the polymer are commonly below  $10^{-2}$  S/cm, and even those containing highly aligned and well-dispersed ultralarge graphene sheets of a few wt % concentration had no exception.<sup>8</sup> In view of this, constructing a 3D interconnected conductive network within the insulating polymer matrix is more efficient to achieve excellent electrical conductivities than those with 2D graphene arrangement.<sup>34</sup>

The electrical conductivities of the composites are plotted as a function of graphene content along the orthogonal directions as shown in Figure 5a. There was a remarkable 9 orders of magnitude increase in electrical conductivity when only 0.25 wt % graphene was added into the epoxy. It should be noted that 0.25 wt %, or an equivalent GO dispersion of 0.3 mg/mL, was the lowest graphene content that could form a GA, and further significantly lowering the GO dispersion concentration was very difficult because the weakly interacted GO sheets could not be assembled into a stable 3D structure. Therefore, the percolation threshold for the GA/epoxy composites in this study was estimated to be slightly lower than 0.25 wt %.<sup>29</sup> It is of interest to notice that the conductivities were almost identical in the orthogonal directions for graphene contents up to about 0.5–0.7 wt %. Above this value, the conductivity was gradually higher in the alignment direction than in the transverse direction, and the disparity in conductivity became larger with increasing graphene content, functionally analogous to a recent study on aligned rGO sheets/epoxy composites.<sup>7</sup> The difference was as high as 0.08 S/cm (see inset in Figure 5a), equivalent to 67% of the value measured in the transverse direction with 1.4 wt % graphene. The anisotropic electrical conductivities at high graphene contents suggest that the alignment of graphene started at approximately 0.5–0.7 wt %, below which the GA structure was random and macroscopically isotropic. A major reason for the much lower conductivity in the transverse direction is due probably to some disconnected paths, especially at the junctions where the horizontal rGO sheets meet the transverse supporting rGO sheets, as highlighted by circles in Figure 5a.

The anisotropic properties of GA/epoxy composites at high graphene content were confirmed using the polarized Raman spectroscopy. This technique has been employed to investigate the alignment of CNTs and graphene in polymer-based composites.<sup>7,47,48</sup> The Raman sensitive bands of CNTs or graphene exhibited a collective resonance when the laser light was focused along the alignment direction, whereas remarkable angle-dependent attenuation of the peaks occurred with the maximum suppression in the direction perpendicular to it.<sup>7,48</sup> The composites with different graphene contents were subjected to scanning of laser lights parallel and transverse to the alignment direction, and the corresponding G- and D-

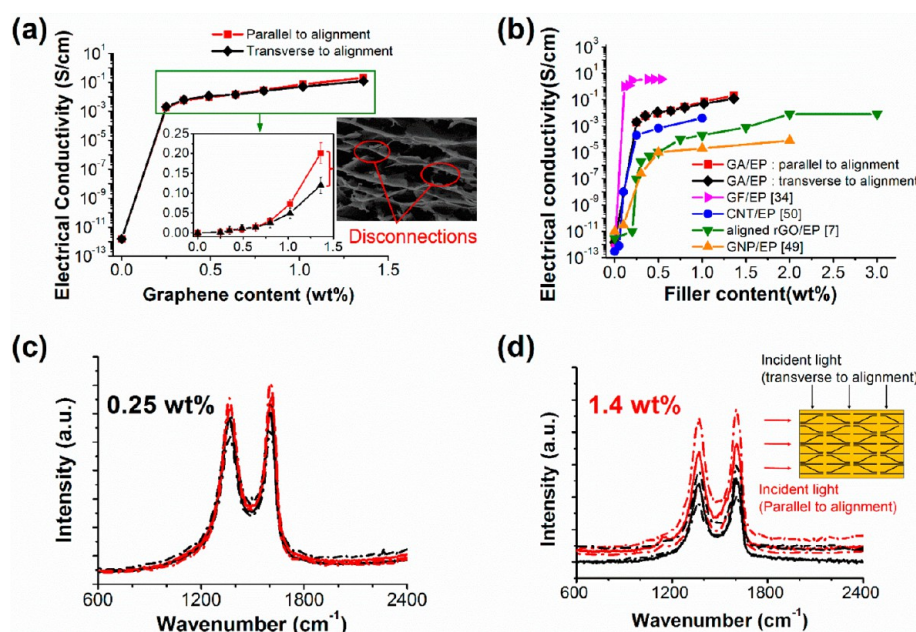


**Figure 5.** (a) Electrical conductivities of GA/epoxy composites in the direction parallel to the alignment and transverse to it; (b) comparison of electrical conductivities of epoxy-based nanocomposites containing graphene and CNTs; and polarized Raman spectra for composites containing (c) 0.25 wt % and (d) 1.4 wt % graphene.

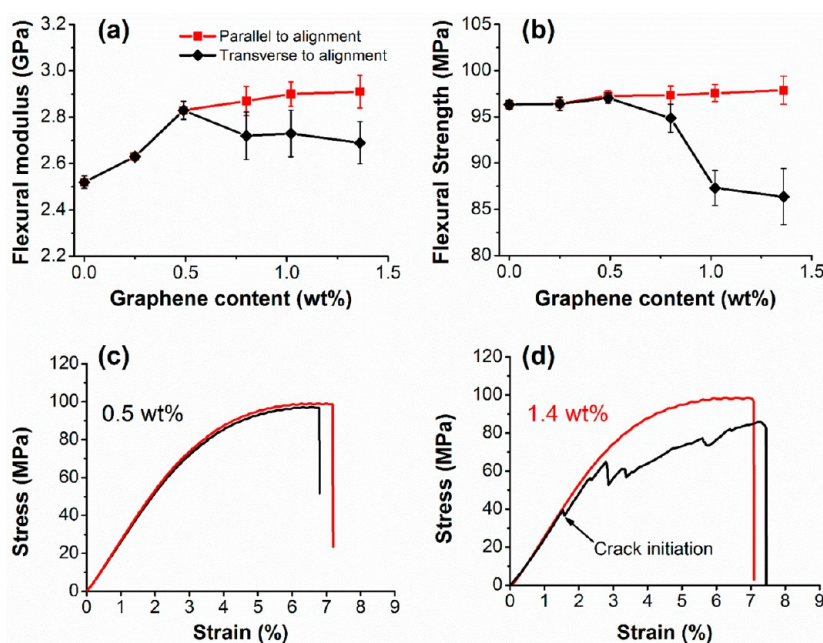


**Figure 6.** (a) Flexural modulus and (b) strength of GA/epoxy composites; typical stress–strain curves of GA/epoxy composites containing (c) 0.5 and (d) 1.4 wt % graphene in orthogonal directions.

bands are shown in Figure 5c and d. In contrast to almost identical Raman spectra in the orthogonal directions for the composites containing 0.25 wt % graphene, which indicated randomly dispersed rGO sheets, the intensities of the Raman G- and D-bands of the composites containing 1.4 wt % graphene were ~44% higher in the alignment direction than that transverse to it. This means that there was higher resonance in the direction parallel to the alignment, confirming significant alignment of rGO layers in the composites.

A comparison of electrical conductivities between the current study and the literature with epoxy-based nanocomposites containing nanocarbon materials, including graphene of various

forms and CNTs, is shown in Figure 5b. The highest conductivity obtained for the GA/epoxy composites in this study was 0.2 S/cm (at 1.4 wt % graphene content), which is 4 orders of magnitude higher than that of 2.0 wt % GNP<sup>49</sup> and nearly 2 orders of magnitude higher than those containing 3 wt % rGO<sup>7</sup> or 1 wt % CNTs.<sup>50</sup> However, the value obtained here is lower than 3.6 S/cm of 0.5 wt % GF/epoxy composites.<sup>34</sup> The difference in conductivity arises from the uniform cellular structure of GF with 100% sp<sup>2</sup> graphitic carbon, whereas GA contained a largely nonuniform porous structure and the carbon was only partially reduced at a moderate temperature. Nevertheless, the excellent electrical conductivities of GA/



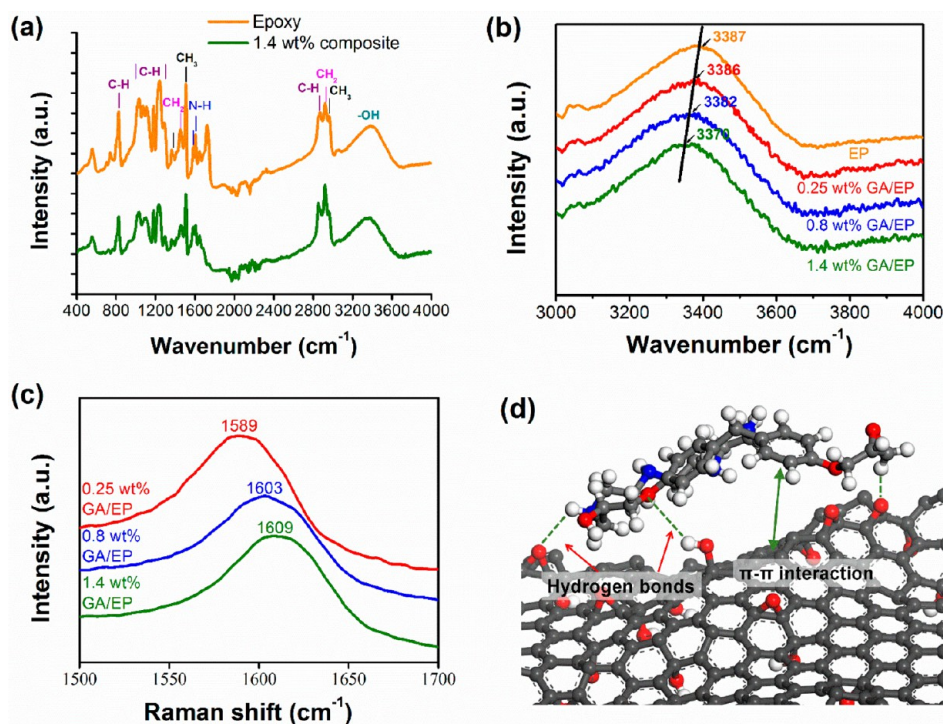


**Figure 7.** FTIR spectra of epoxy and GA/epoxy composites (a) in 400–4000  $\text{cm}^{-1}$  and (b) showing the vibration of  $\text{—OH}$  at wavenumbers 3000–3700  $\text{cm}^{-1}$ , (c) Raman G-band peak, and (d) schematic of interfacial bonding mechanisms of GA/epoxy composites.

epoxy composites are a testament to a higher efficiency of the 3D interconnected graphene structure in forming conductive networks than any other forms of carbon materials. GAs have a good potential to further enhance the electrical conductivity by increasing the precursor GO content and full reduction.

**3.4. Flexural Properties and Fracture Toughness of GA/Epoxy Composites.** The flexural properties of GA/epoxy composites are plotted as a function of graphene content in Figure 6. The flexural modulus in the alignment direction increased by about 12% with 0.5 wt % graphene, and a further increase in graphene content resulted in only a marginal increase or saturation. Nevertheless, the modulus measured in the transverse direction showed a peak at 0.5 wt % graphene, followed by gradual reductions at higher graphene contents. It is of interest to note that the flexural strength showed essentially the same trend as the flexural modulus in both directions, although the increase of strength due to a higher graphene content was quite limited.

In view of the fact that the transition both in flexural modulus and strength occurred after 0.5 wt % graphene, it can be said the reinforcing efficiency by graphene started to decrease in the transverse direction at this juncture. A functionally very similar transition in electrical conductivity was observed at the very similar graphene content of 0.5–0.7 wt % (Figure 5a). A major difference is that the electrical conductivity never decreased with increasing graphene concentration beyond this transition point because of the more interconnected rGO sheets even in the transverse direction.

To explore the effects of graphene content on mechanical properties, typical stress–strain curves of GA/epoxy composites containing 0.5 and 1.4 wt % graphene are specifically studied, as shown in Figures 6c,d. The curves corresponding to 0.5 wt % graphene presented essentially the same stable loading behavior in the two orthogonal directions without apparent damage until catastrophic failure at  $\sim 7\%$  strain (Figure 6c).

The almost isotropic mechanical properties of the composites with graphene contents up to  $\sim 0.5$  wt % resulted from the porous structure of GAs with no particular directionality (Figure 1b). In sharp contrast, the composites containing 1.4 wt % graphene exhibited distinct stress–strain curves between the two orthogonal directions. As compared to the stable loading behavior in the alignment direction, there was an early crack initiation in the transverse direction after about 1.5% strain, followed by stick–slip crack propagation before failure at about 7.5% strain. The stick–slip stress–strain behavior indicates intermittent damage accumulation, leading to a reduction in load-carrying capacity before the final failure of the composites.

The gradual degradation of strength and modulus in the transverse direction beyond the transitional graphene content of 0.5 wt % is analogous to the well-known transverse properties of unidirectional fiber composites containing 60–65 vol % continuous fibers. Their transverse moduli are generally higher than that of the matrix material, but lower than those measured in the longitudinal direction as the simple rule of mixtures equations can predict. Their transverse strengths are even much lower than that of the matrix material, and the higher is the fiber content, the lower is the transverse strength.<sup>51</sup> In fiber reinforced composites under transverse loading, the fiber–matrix interfaces are the weakest links and thus function as defects, leading to premature crack initiation and failure.<sup>52</sup> By the similar token, the aligned rGO sheets can be considered as defects that may cause premature failure by crack propagation directly through the rGO–epoxy interface or between the loosely assembled rGO layers when the GA/epoxy composite is subjected to transverse loading. With increasing graphene content, increasingly more rGO sheets are aligned in one direction, resulting in easier propagation of the premature cracks (see section 3.5 and Figure 9i for further discussion on fracture behavior).



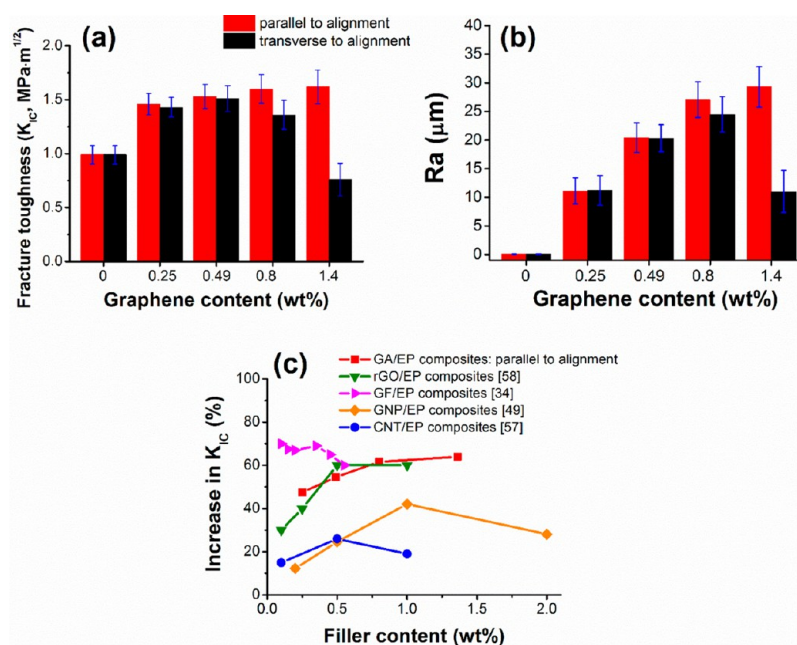


**Figure 8.** (a) Mode I fracture toughness,  $K_{IC}$ , and (b) fracture surface roughness,  $R_a$ , plotted as a function of graphene content; and (c) comparison of fracture toughness between epoxy-based nanocomposites containing different carbon materials.

It is well-known that the strength of graphene composites is significantly affected by the interfacial adhesion.<sup>53</sup> To characterize the interfacial bonding mechanism in GA/epoxy composites, FTIR and Raman spectroscopy were studied, as shown in Figure 7a–c. The FTIR spectrum of the neat epoxy showed several characteristic absorption bands: the bands at 1580 and 1606  $\text{cm}^{-1}$  are assigned to N–H bending, whereas the bands at 1510, 1383, and 1460  $\text{cm}^{-1}$  are associated with the deformation vibration mode of  $\text{CH}_3$  (first two bands) and  $\text{CH}_2$  (last band), respectively. The asymmetrical C–H stretching for  $\text{CH}_3$  and  $\text{CH}_2$  absorption appears at 2964 and 2929  $\text{cm}^{-1}$ . The aldehyde C–H stretching and C–H out of plane deformation are assigned to 2864 and 829  $\text{cm}^{-1}$ . The substitution patterns on the aromatic ring can be judged from the out-of-plane bending of the ring C–H bond, leading to the formation of prominent peaks in the region 1000–1300  $\text{cm}^{-1}$ , due to the chemical reaction between the curing agent and epoxy.<sup>54</sup> The broad and strong absorption at 3000–3700  $\text{cm}^{-1}$  (highlighted in Figure 7b) is attributed to the symmetrical stretching vibration of hydroxyl groups in epoxy. The GA/epoxy composites exhibited a FTIR spectrum quite similar to that of the neat epoxy, except for a downshift of the hydroxyl peak from 3387 to 3370  $\text{cm}^{-1}$ , indicating the existence of hydrogen bonds between the oxygenated functional groups of rGO and the hydroxyl groups on the epoxy molecules.<sup>55,56</sup> Apart from the hydrogen bonds, the  $\pi$ – $\pi$  interaction was operational between the aromatic rings of the graphitic segments,<sup>7</sup> which in turn led to a slight upshift in the Raman G-band (Figure 7c). However, there was no evidence suggesting the presence of covalent bonds. Therefore, it can be concluded that the interfacial bonding in the GA/epoxy composites was mainly noncovalent, including hydrogen bonds and  $\pi$ – $\pi$  interaction. These bonding mechanisms of GA/epoxy composites are schematically presented in Figure 7d. The weak noncovalent bonds explained the limited increase in mechanical properties, especially the flexural strength of the GA/epoxy composites (Figure 6b).

Although GA had marginal strengthening and stiffening effects on flexural properties of the composites, it significantly ameliorated the quasi-static fracture toughness, as shown in Figure 8a. Unlike the modulus and strength, the  $K_{IC}$  value of the composites in the alignment direction (with a crack propagating perpendicular to the alignment) increased sharply from 0.99 to 1.46  $\text{MPa m}^{1/2}$  with only 0.25 wt % graphene, corresponding to a remarkable enhancement of over 47% as compared to the neat epoxy. A further increase in graphene content resulted in a marginal increase in  $K_{IC}$ , leading to a total of 64% improvement with 1.4 wt % graphene. In contrast, however, the  $K_{IC}$  value of the same composites in the transverse direction presented a totally different behavior: it initially increased similar to that measured in the alignment direction for graphene content up to 0.5 wt %, followed by drastic drops as the graphene content further increased, thus showing even 23% lower fracture toughness than that of the neat epoxy at 1.4 wt % graphene. Again, this observation is very similar to the flexural properties shown in Figure 6, with the transition of the properties between the two directions occurring consistently at about 0.5 wt % graphene. Therefore, when comparing the fracture toughness measured in the two directions, an astonishing 113% disparity was revealed, which is much larger than the corresponding difference in flexural modulus or strength.

The comparison of the fracture surfaces clearly suggests gradual changes in surface roughness when the graphene content was increased. Indeed, the surface roughness values measured of the composites with cracks propagating parallel and transverse to the alignment directions further confirmed this hypothesis, as shown in Figure 8b. The  $R_a$  value drastically increased by almost 500 times, from  $\sim 60$  nm for the neat epoxy to  $\sim 30$   $\mu\text{m}$  after incorporating 1.4 wt % graphene in the alignment direction, whereas the  $R_a$  values of the composites fractured in the transverse direction were generally lower. Essentially, the surface roughness followed very much the same trend as the fracture toughness for both directions (Figure 8a).

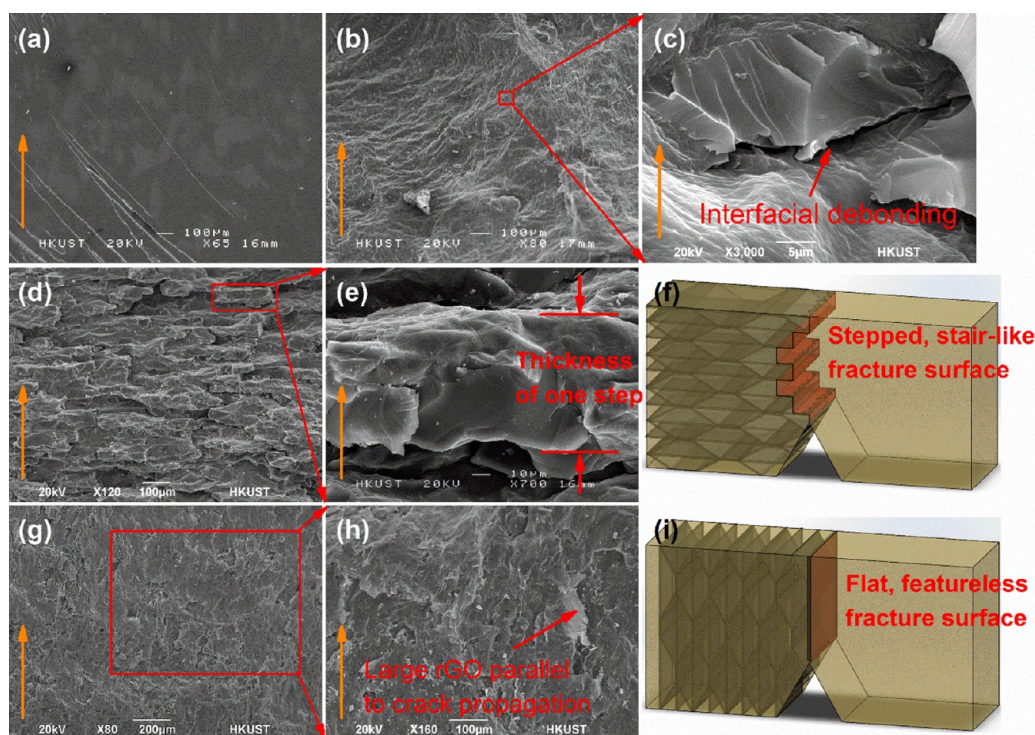


**Figure 9.** SEM images of the fracture surfaces of SENB test specimens for (a) neat epoxy and GA/EP composites with graphene contents (b,c) 0.25 wt %; (d–i) 1.4 wt %: cracks propagating (d,e) against the alignment direction and (g,h) along the alignment direction; and (f,i) schematics of crack propagation process. Orange arrows indicate the direction of crack propagation.

This analogy indicates that the fracture surface roughness reflects the amount of the energy absorbed during fracture and can be used as a measure of fracture toughness of graphene/epoxy composites.<sup>34</sup>

The fracture toughness values of epoxy-based nanocomposites containing graphene and CNTs taken from the literature are compared to the present study in Figure 8c. For CNT/epoxy composites, the increase in  $K_{IC}$  was typically unimpressive, delivering only 25% improvement with 0.5 wt % CNTs.<sup>57</sup> Graphene-based composites exhibited generally better performance: GNP and rGO/epoxy composites showed 40–53% improvements, respectively.<sup>49,58</sup> Benefiting from the interconnected cellular structure, the GF/epoxy composites delivered an outstanding fracture toughness of 70% enhancement against the neat epoxy with only 0.1 wt % graphene, which was among the best results thus far reported.<sup>34</sup> The absolute values of  $K_{IC}$  data used in Figure 8b from the references can be found in the Supporting Information. Our result with 64% improvement at 1.4 wt % graphene stands between these two outstanding outcomes, and the comparison indicates that the 3D interconnected GA is in general much more effective in improving the fracture toughness of composites than either 1D CNTs or 2D graphene sheets.

**3.5. Toughening Mechanisms.** The SEM images of the fracture surfaces of the neat epoxy and GA/epoxy composites are shown in Figure 9 to study the toughening mechanisms. The fracture surface of the neat epoxy displayed a smooth and featureless surface, which is typical of brittle fracture of homogeneous thermoset polymers, indicating very weak resistance to crack propagation. In search of toughening mechanisms relevant to the present GA/epoxy composites, the following discussion is made with reference to well-established mechanisms in nanocomposites.

Crack pinning is one of the most important failure mechanisms in CNT and graphene/epoxy composites and is normally manifested by crack front bowing when resisted by the rigid nanofillers.<sup>35,59</sup> However, no solid evidence of such crack pinning was found in the present GA/epoxy composites. A possible explanation is that unlike the composites reinforced in isolation with individual or bundled carbon nanotubes or graphene sheets, the cracks in GA composites cannot bypass or bow out through the 3D interconnected rGO layers. They have to break or overcome the interconnected walls consisting of multilayer rGO sheets if they were to propagate. The consequence is that the crack tip was blunted and deflected upon encountering the rGO walls, leaving behind significantly increased fracture surface area with rough surface, leading to greater energy absorption than in the neat polymer.<sup>57,59</sup>

At a low graphene content (Figure 9b and c), the GA/epoxy interfacial debonding may have contributed significantly to fracture energy absorption of the composites. The debonding was caused by the moderate interfacial adhesion arising from the noncovalent bonding mechanisms like hydrogen bonds and  $\pi$ – $\pi$  interaction operating at the interface without particular functionalization of rGO.<sup>9,53</sup> At high graphene contents, crack tip blunting and deflection by breaking the graphene walls became an important mechanism of the composites. The fracture surface shown in Figure 9d presents a “stair-like” feature where the cracks were deflected step by step when they reached the layered structure consisting of horizontally aligned rGO sheets. The higher magnification SEM image (Figure 9e) highlights the step of the “stair-like” fracture surface, whose thickness is similar to the distance between the two adjacent aligned rGO layers (Figure 1d). A possible scenario occurring in the GA/epoxy composites when the crack grows transverse to the alignment is illustrated in Figure 9f. The horizontally



aligned rGO sheets can severely obstruct crack propagation, leading to stepped crack deflections in a staggered manner, causing a change in the stress state from mode I to mix modes, which requires more energy to dissipate, thus resulting in a higher fracture toughness.<sup>34,60</sup> In stark contrast, when the composites were loaded with a crack propagating along the alignment direction, a flat and featureless fracture surface was shown (Figure 9g) as a result of easy crack growth along the moderately bonded interface between rGO and epoxy or through the weakly bonded rGO layers. This observation is further proven by the large rGO sheets exposed on the fracture surface parallel to the crack propagation direction (Figure 9h). The corresponding fracture process is illustrated in Figure 9i.

Therefore, the major roles of the 3D interconnected rGO reinforcement at high graphene content in improving the fracture toughness of GA/epoxy composites can be summarized as follows. (i) A huge amount of energy is dissipated when the cracks have to overcome or break the rGO walls of the 3D interconnected GA; (ii) crack deflection caused by well-aligned rGO layers requires a large driving force, leading to an enhanced fracture toughness; and (iii) debonding along the GA/epoxy interface or through the rGO multisheets contributes to a less extent to energy absorption when the crack propagates along the alignment direction.

#### 4. CONCLUSION

We report the fabrication of GAs through one-step chemical reduction and self-assembly of GO sheets with HI acid, followed by freeze-drying. Composites were prepared by infiltrating GA with liquid epoxy resin under vacuum. The composites delivered significant anisotropic properties in two in-plane perpendicular directions with remarkable electrical conductivities, excellent mechanical properties, and fracture toughness. The following can be highlighted from the study:

(i) The GAs made from high concentration rGO sheets possessed a 3D interconnected layered structure, consisting of long horizontal layers, which were vertically connected by shorter bridges. The layered structure was formed due to the synergy of several mechanisms including large-size GO sheets, low viscosity aqueous system, steric hindrance between the rGO sheets, the excluded volume principle, and the anisotropic growth of the ice crystals. The layered structure was highly stable and flexible, capable of bearing up to 90% strain without fracture under cyclic compression, resulting from the flexible joints and an extremely high porosity.

(ii) The GO sheets were reduced during the GA fabrication process, giving rise to a reduction in Raman  $I_D/I_G$  ratio, downshift of Raman G-band, and a drastically increased C/O ratio. The resulting GA showed remarkable electrical conductivities of 0.04–0.25 S/cm depending on the concentration of rGO, which further proved almost full recovery of the conductivity after reduction.

(iii) The layered structure of GA offered the composites unusual anisotropic mechanical and electrical properties between the directions of alignment and that transverse to it above a transition point of 0.5 wt %: the properties measured parallel to the alignment were progressively higher with an increase of graphene content than those measured transverse to the alignment.

(iv) The electrical conductivity of the composite was a remarkable  $2 \times 10^{-3}$  S/cm with only 0.25 wt % graphene, much higher than those of the composites made by direct dispersion of GNPs or rGO sheets into the polymer. However, the

incorporation of GA resulted in marginal effects on strength and modulus of the composites due to the moderate interfacial adhesion between the rGO without prior functionalization and the epoxy matrix.

(v) A remarkable 64% enhancement in fracture toughness of the composites as compared to the neat epoxy was achieved at 1.4 wt % graphene content. Breakage of 3D interconnected GA structure, interfacial debonding, and crack deflection were mainly responsible for the enhanced fracture toughness, which are reflected by the “stair-like” feature and the gradually larger fracture surface roughness with increasing graphene content.

It is challenging to design materials with concurrent improvements in both strength and fracture toughness because they are often mutually exclusive, and in most cases one property has to be sacrificed for the sake of the other.<sup>52</sup> However, we demonstrated in this work that significant improvements in both conductivity and fracture toughness were achieved by introducing 3D interconnected GA into an epoxy matrix without sacrificing the mechanical strength. Even with the 3D structure of GA, we were able to rationally design the composites to introduce significant anisotropy in these properties between the in-plane directions parallel and transverse to alignment. There is a significant analogy between the composites reinforced by 3D GA and fiber reinforced laminates in terms of their high fracture resistance to suppress crack propagation along a certain direction. The anisotropic electrical properties of GA/epoxy composites can be applied in many areas such as anisotropic conductive adhesives requiring most of the currents to flow in one direction.<sup>31</sup> Besides, the anisotropic structure of GA has the potential for reinforcement in biological composites by incorporating biocompatible polymers, such as the outer structure in multilayered biological systems where the anisotropy serves to direct crack propagation, stress, and energy dissipation to greater depths into underlying more ductile materials.<sup>32</sup>

#### ■ ASSOCIATED CONTENT

##### Supporting Information

Detailed synthesis method of GA/epoxy composites, area distributions of GO sheets and their typical SEM images, full XPS spectra of GA before and after washing with water, XPS I 3d<sub>5/2</sub> deconvoluted peaks and the chemical composition of GA before washing with water, and absolute fracture toughness values of epoxy-based nanocomposites containing graphene and CNTs taken from the literature. This material is available free of charge via the Internet at <http://pubs.acs.org>.

#### ■ AUTHOR INFORMATION

##### Corresponding Author

\*Tel.: +852 2358 7207. Fax: +852 2358 1543. E-mail: mejjkim@ust.hk.

##### Notes

The authors declare no competing financial interest.

#### ■ ACKNOWLEDGMENTS

The project was supported by the Research Grants Council of Hong Kong SAR. Z.W. and X.S. were recipients of the Hong Kong Ph.D. Fellowship. Technical assistance from the Materials Characterization and Preparation Facilities (MCPF), Advanced Engineering Materials Facilities (AEMF), the Department of Chemical and Biomolecular Engineering at HKUST, and the



Department of Physics and Materials Science at the City University of Hong Kong is appreciated.

## REFERENCES

- (1) Geim, A. K.; Novoselov, K. S. The Rise of Graphene. *Nat. Mater.* **2007**, *6*, 183–191.
- (2) Rao, C. N. R.; Sood, A. K.; Subrahmanyam, K. S.; Govindaraj, A. Graphene: The New Two-Dimensional Nanomaterial. *Angew. Chem., Int. Ed.* **2009**, *48*, 7752–7777.
- (3) Stankovich, S.; Dikin, D. A.; Dommett, G. H. B.; Kohlhaas, K. M.; Zimney, E. J.; Stach, E. A.; Piner, R. D.; Nguyen, S. T.; Ruoff, R. S. Graphene-Based Composite Materials. *Nature* **2006**, *442*, 282–286.
- (4) Song, P.; Cao, Z.; Cai, Y.; Zhao, L.; Fang, Z.; Fu, S. Fabrication of Exfoliated Graphene-Based Polypropylene Nanocomposites with Enhanced Mechanical and Thermal Properties. *Polymer* **2011**, *52*, 4001–4010.
- (5) Yan, J.; Wei, T.; Shao, B.; Fan, Z.; Qian, W.; Zhang, M.; Wei, F. Preparation of a Graphene Nanosheet/polyaniline Composite with High Specific Capacitance. *Carbon* **2010**, *48*, 487–493.
- (6) Zhang, H.-B.; Zheng, W.-G.; Yan, Q.; Jiang, Z.-G.; Yu, Z.-Z. The Effect of Surface Chemistry of Graphene on Rheological and Electrical Properties of Polymethylmethacrylate Composites. *Carbon* **2012**, *50*, S117–S125.
- (7) Yousefi, N.; Lin, X.; Zheng, Q.; Shen, X.; Pothnis, J. R.; Jia, J.; Zussman, E.; Kim, J.-K. Simultaneous in Situ Reduction, Self-Alignment and Covalent Bonding in Graphene Oxide/epoxy Composites. *Carbon* **2013**, *59*, 406–417.
- (8) Yousefi, N.; Sun, X.; Lin, X.; Shen, X.; Jia, J.; Zhang, B.; Tang, B.; Chan, M.; Kim, J.-K. Highly Aligned Graphene/polymer Nanocomposites with Excellent Dielectric Properties for High-Performance Electromagnetic Interference Shielding. *Adv. Mater.* **2014**, *26*, 5480–5487.
- (9) Tang, L.-C.; Wan, Y.-J.; Yan, D.; Pei, Y.-B.; Zhao, L.; Li, Y.-B.; Wu, L.-B.; Jiang, J.-X.; Lai, G.-Q. The Effect of Graphene Dispersion on the Mechanical Properties of Graphene/epoxy Composites. *Carbon* **2013**, *60*, 16–27.
- (10) Hu, H.; Wang, X.; Wang, J.; Wan, L.; Liu, F.; Zheng, H.; Chen, R.; Xu, C. Preparation and Properties of Graphene Nanosheets–polystyrene Nanocomposites via in Situ Emulsion Polymerization. *Chem. Phys. Lett.* **2010**, *484*, 247–253.
- (11) Shim, S. H.; Kim, K. T.; Lee, J. U.; Jo, W. H. Facile Method to Functionalize Graphene Oxide and Its Application to Poly(ethylene Terephthalate)/graphene Composite. *ACS Appl. Mater. Interfaces* **2012**, *4*, 4184–4191.
- (12) Li, W.; Tang, X.-Z.; Zhang, H.-B.; Jiang, Z.-G.; Yu, Z.-Z.; Du, X.-S.; Mai, Y.-W. Simultaneous Surface Functionalization and Reduction of Graphene Oxide with Octadecylamine for Electrically Conductive Polystyrene Composites. *Carbon* **2011**, *49*, 4724–4730.
- (13) Chen, Z.; Ren, W.; Gao, L.; Liu, B.; Pei, S.; Cheng, H.-M. Three-Dimensional Flexible and Conductive Interconnected Graphene Networks Grown by Chemical Vapour Deposition. *Nat. Mater.* **2011**, *10*, 424–428.
- (14) Chabot, V.; Higgins, D.; Yu, A.; Xiao, X.; Chen, Z.; Zhang, J. A Review of Graphene and Graphene Oxide Sponge: Material Synthesis and Applications to Energy and the Environment. *Energy Environ. Sci.* **2014**, *7*, 1564–1596.
- (15) Cao, X.; Yin, Z.; Zhang, H. Three-Dimensional Graphene Materials: Preparation, Structures and Application in Supercapacitors. *Energy Environ. Sci.* **2014**, *7*, 1850–1865.
- (16) Nardecchia, S.; Carriazo, D.; Ferrer, M. L.; Gutiérrez, M. C.; del Monte, F. Three Dimensional Macroporous Architectures and Aerogels Built of Carbon Nanotubes And/or Graphene: Synthesis and Applications. *Chem. Soc. Rev.* **2013**, *42*, 794–830.
- (17) Zhang, X.; Sui, Z.; Xu, B.; Yue, S.; Luo, Y.; Zhan, W.; Liu, B. Mechanically Strong and Highly Conductive Graphene Aerogel and Its Use as Electrodes for Electrochemical Power Sources. *J. Mater. Chem.* **2011**, *21*, 6494–6497.
- (18) Bai, H.; Li, C.; Wang, X.; Shi, G. On the Gelation of Graphene Oxide. *J. Phys. Chem. C* **2011**, *115*, 5545–5551.
- (19) Worsley, M. A.; Pauzauskie, P. J.; Olson, T. Y.; Biener, J.; Satcher, J. H.; Baumann, T. F. Synthesis of Graphene Aerogel with High Electrical Conductivity. *J. Am. Chem. Soc.* **2010**, *132*, 14067–14069.
- (20) Xu, Y.; Sheng, K.; Li, C.; Shi, G. Self-Assembled Graphene Hydrogel via a One-Step Hydrothermal Process. *ACS Nano* **2010**, *4*, 4324–4330.
- (21) Xu, Y.; Lin, Z.; Huang, X.; Liu, Y.; Huang, Y.; Duan, X. Flexible Solid-State Supercapacitors Based on Three-Dimensional Graphene Hydrogel Films. *ACS Nano* **2013**, *7*, 4042–4049.
- (22) Zhang, L.; Shi, G. Preparation of Highly Conductive Graphene Hydrogels for Fabricating Supercapacitors with High Rate Capability. *J. Phys. Chem. C* **2011**, *115*, 17206–17212.
- (23) Hu, H.; Zhao, Z.; Wan, W.; Gogotsi, Y.; Qiu, J. Ultralight and Highly Compressible Graphene Aerogels. *Adv. Mater.* **2013**, *25*, 2219–2223.
- (24) Qian, Y.; Ismail, I. M.; Stein, A. Ultralight, High-Surface-Area, Multifunctional Graphene-Based Aerogels from Self-Assembly of Graphene Oxide and Resol. *Carbon* **2014**, *68*, 221–231.
- (25) Qiu, L.; Liu, D.; Wang, Y.; Cheng, C.; Zhou, K.; Ding, J.; Truong, V.-T.; Li, D. Mechanically Robust, Electrically Conductive and Stimuli-Responsive Binary Network Hydrogels Enabled by Superelastic Graphene Aerogels. *Adv. Mater.* **2014**, *26*, 3333–3337.
- (26) Ye, S.; Feng, J.; Wu, P. Highly Elastic Graphene Oxide–epoxy Composite Aerogels via Simple Freeze-Drying and Subsequent Routine Curing. *J. Mater. Chem. A* **2013**, *1*, 3495–3502.
- (27) Hu, H.; Zhao, Z.; Wan, W.; Gogotsi, Y.; Qiu, J. Polymer/graphene Hybrid Aerogel with High Compressibility, Conductivity, and “Sticky” Superhydrophobicity. *ACS Appl. Mater. Interfaces* **2014**, *6*, 3242–3249.
- (28) Tang, G.; Jiang, Z.-G.; Li, X.; Zhang, H.-B.; Dasari, A.; Yu, Z.-Z. Three Dimensional Graphene Aerogels and Their Electrically Conductive Composites. *Carbon* **2014**, *77*, 592–599.
- (29) Irin, F.; Das, S.; Atore, F. O.; Green, M. J. Ultralow Percolation Threshold in Aerogel and Cryogel Templated Composites. *Langmuir* **2013**, *29*, 11449–11456.
- (30) Zhong, Y.; Zhou, M.; Huang, F.; Lin, T.; Wan, D. Effect of Graphene Aerogel on Thermal Behavior of Phase Change Materials for Thermal Management. *Sol. Energy Mater. Sol. Cells* **2013**, *113*, 195–200.
- (31) Lin, Y. C.; Zhong, J. A Review of the Influencing Factors on Anisotropic Conductive Adhesives Joining Technology in Electrical Applications. *J. Mater. Sci.* **2008**, *43*, 3072–3093.
- (32) Han, L.; Wang, L.; Song, J.; Boyce, M. C.; Ortiz, C. Direct Quantification of the Mechanical Anisotropy and Fracture of an Individual Exoskeleton Layer via Uniaxial Compression of Micropillars. *Nano Lett.* **2011**, *11*, 3868–3874.
- (33) Jia, J.; Kan, C.-M.; Lin, X.; Shen, X.; Kim, J.-K. Effects of Processing and Material Parameters on Synthesis of Monolayer Ultralarge Graphene Oxide Sheets. *Carbon* **2014**, *77*, 244–254.
- (34) Jia, J.; Sun, X.; Lin, X.; Shen, X.; Mai, Y.-W.; Kim, J.-K. Exceptional Electrical Conductivity and Fracture Resistance of 3D Interconnected Graphene Foam/Epoxy Composites. *ACS Nano* **2014**, *8*, 5774–5783.
- (35) Chandrasekaran, S.; Sato, N.; Tölle, F.; Mülhaupt, R.; Fiedler, B.; Schulte, K. Fracture Toughness and Failure Mechanism of Graphene Based Epoxy Composites. *Compos. Sci. Technol.* **2014**, *97*, 90–99.
- (36) Lin, X.; Shen, X.; Zheng, Q.; Yousefi, N.; Ye, L.; Mai, Y.-W.; Kim, J.-K. Fabrication of Highly-Aligned, Conductive, and Strong Graphene Papers Using Ultralarge Graphene Oxide Sheets. *ACS Nano* **2012**, *6*, 10708–10719.
- (37) Aboutalebi, S. H.; Gudarzi, M. M.; Zheng, Q. B.; Kim, J.-K. Spontaneous Formation of Liquid Crystals in Ultralarge Graphene Oxide Dispersions. *Adv. Funct. Mater.* **2011**, *21*, 2978–2988.
- (38) Yousefi, N.; Gudarzi, M. M.; Zheng, Q.; Lin, X.; Shen, X.; Jia, J.; Sharif, F.; Kim, J.-K. Highly Aligned, Ultralarge-Size Reduced Graphene Oxide/polyurethane Nanocomposites: Mechanical Properties and Moisture Permeability. *Composites, Part A* **2013**, *49*, 42–50.

- (39) Li, W. L.; Lu, K.; Walz, J. Y. Freeze Casting of Porous Materials: Review of Critical Factors in Microstructure Evolution. *Int. Mater. Rev.* **2012**, *57*, 37–60.
- (40) Pei, S.; Zhao, J.; Du, J.; Ren, W.; Cheng, H.-M. Direct Reduction of Graphene Oxide Films into Highly Conductive and Flexible Graphene Films by Hydrohalic Acids. *Carbon* **2010**, *48*, 4466–4474.
- (41) Gibson, L. J. Biomechanics of Cellular Solids. *J. Biomech.* **2005**, *38*, 377–399.
- (42) Li, J.; Li, J.; Meng, H.; Xie, S.; Zhang, B.; Li, L.; Ma, H.; Zhang, J.; Yu, M. Ultra-Light, Compressible and Fire-Resistant Graphene Aerogel as a Highly Efficient and Recyclable Absorbent for Organic Liquids. *J. Mater. Chem. A* **2014**, *2*, 2934–2941.
- (43) Tao, Y.; Kong, D.; Zhang, C.; Lv, W.; Wang, M.; Li, B.; Huang, Z. H.; Kang, F.; Yang, Q. H. Monolithic Carbons with Spheroidal and Hierarchical Pores Produced by the Linkage of Functionalized Graphene Sheets. *Carbon* **2014**, *69*, 169–177.
- (44) Chua, C. K.; Pumera, M. Chemical Reduction of Graphene Oxide: A Synthetic Chemistry Viewpoint. *Chem. Soc. Rev.* **2014**, *43*, 291–312.
- (45) Pham, H. D.; Pham, V. H.; Cuong, T. V.; Nguyen-Phan, T.-D.; Chung, J. S.; Shin, E. W.; Kim, S. Synthesis of the Chemically Converted Graphene Xerogel with Superior Electrical Conductivity. *Chem. Commun.* **2011**, *47*, 9672–9674.
- (46) Wang, Z.; Wang, W.; Wang, M.; Meng, X.; Li, J. P-Type Reduced Graphene Oxide Membranes Induced by Iodine Doping. *J. Mater. Sci.* **2013**, *48*, 2284–2289.
- (47) Wang, Q.; Dai, J.; Li, W.; Wei, Z.; Jiang, J. The Effects of CNT Alignment on Electrical Conductivity and Mechanical Properties of SWNT/epoxy Nanocomposites. *Compos. Sci. Technol.* **2008**, *68*, 1644–1648.
- (48) Haggmueller, R.; Gommans, H. H.; Rinzler, A. G.; Fischer, J. E. Aligned Single-Wall Carbon Nanotubes in Composites by Melt Processing Methods. *Chem. Phys. Lett.* **2000**, *330*, 219–225.
- (49) Chandrasekaran, S.; Seidel, C.; Schulte, K. Preparation and Characterization of Graphite Nano-Platelet (GNP)/epoxy Nano-Composite: Mechanical, Electrical and Thermal Properties. *Eur. Polym. J.* **2013**, *49*, 3878–3888.
- (50) Li, J.; Ma, P. C.; Chow, W. S.; To, C. K.; Tang, B. Z.; Kim, J.-K. Correlations between Percolation Threshold, Dispersion State, and Aspect Ratio of Carbon Nanotubes. *Adv. Funct. Mater.* **2007**, *17*, 3207–3215.
- (51) Hull, D.; Clyne, T. W. *An Introduction to Composite Materials*, 2nd ed.; Cambridge University Press: London, 1996.
- (52) Kim, J. K.; Mai, Y. W. *Engineered Interfaces in Fiber Reinforced Composites*; Elsevier: Oxford, 1998; p 185.
- (53) Li, J.; Sham, M. L.; Kim, J.-K.; Marom, G. Morphology and Properties of UV/Ozone Treated Graphite Nanoplatelet/epoxy Nanocomposites. *Compos. Sci. Technol.* **2007**, *67*, 296–305.
- (54) Chan, M.-L.; Lau, K.-T.; Wong, T. T.; Cardona, F. Interfacial Bonding Characteristic of Nanoclay/polymer Composites. *Appl. Surf. Sci.* **2011**, *258*, 860–864.
- (55) Bao, C.; Guo, Y.; Song, L.; Hu, Y. Poly(vinyl Alcohol) Nanocomposites Based on Graphene and Graphite Oxide: A Comparative Investigation of Property and Mechanism. *J. Mater. Chem.* **2011**, *21*, 13942–13950.
- (56) Huang, H.-D.; Ren, P.-G.; Chen, J.; Zhang, W.-Q.; Ji, X.; Li, Z.-M. High Barrier Graphene Oxide Nanosheet/poly(vinyl Alcohol) Nanocomposite Films. *J. Membr. Sci.* **2012**, *409–410*, 156–163.
- (57) Ayatollahi, M. R.; Shadlou, S.; Shokrieh, M. M. Fracture Toughness of Epoxy/multi-Walled Carbon Nanotube Nano-Composites under Bending and Shear Loading Conditions. *Mater. Des.* **2011**, *32*, 2115–2124.
- (58) Bortz, D. R.; Heras, E. G.; Martin-Gullon, I. Impressive Fatigue Life and Fracture Toughness Improvements in Graphene Oxide/Epoxy Composites. *Macromolecules* **2012**, *45*, 238–245.
- (59) Sun, L.; Gibson, R. F.; Gordaninejad, F.; Suhr, J. Energy Absorption Capability of Nanocomposites: A Review. *Compos. Sci. Technol.* **2009**, *69*, 2392–2409.
- (60) Bortz, D. R.; Merino, C.; Martin-Gullon, I. Carbon Nanofibers Enhance the Fracture Toughness and Fatigue Performance of a Structural Epoxy System. *Compos. Sci. Technol.* **2011**, *71*, 31–38.